




# Synthesis and characterization of phase-stabilized $\text{Gd}_2\text{FeMnO}_6$ double-Perovskite compound

J. Stella Punitha<sup>1</sup>, A. Nataraj<sup>1</sup>, V. Anbarasu<sup>2</sup>, M. Dhilip<sup>1</sup>, and K. Saravana Kumar<sup>3,\*</sup> 

<sup>1</sup>Department of Physics, SRM Institute of Science & Technology, Ramapuram Campus, Chennai, Tamil Nadu 600 089, India

<sup>2</sup>Department of Physics (Unaided), PSG College of Arts & Science, Coimbatore, Tamil Nadu 641 014, India

<sup>3</sup>Department of Physics, Sri S. Ramasamy Naidu Memorial College, Sattur, Tamil Nadu 626 203, India

Received: 19 December 2020

Accepted: 4 March 2021

Published online:

23 March 2021

© The Author(s), under exclusive licence to Springer Science+Business Media, LLC, part of Springer Nature 2021

## ABSTRACT

In the recent past, a series of double-perovskite compounds with the molecular formula of  $\text{A}_2\text{BB}'\text{O}_6$  have gained keen interest among other inorganic compounds. It is due to the fact that the exhibition of large variety of physical properties pertaining to the elements accommodated at A, B and B' sites. In connection to the preparation of  $\text{Gd}_2\text{FeMnO}_6$ , a novel single-phased double perovskite compound has been carried out using conventional solid-state reaction route. Rietveld refinement of powder XRD patterns reveals that the compound crystallizes in orthorhombic crystal structure with a space group *Pbnm*. X-ray photoelectron spectroscopy analysis confirms the presence of Mn and Fe ions in +3 oxidation state. The field emission scanning electron micrograph reveals the granular growth morphology, having grains with irregular shape with the average grain size of about 5–10  $\mu\text{m}$ . Room-temperature magnetization measurement reveals the dominant antiferromagnetic behaviour with weak ferromagnetic interactions. Deconvoluted Raman spectra using Lorentzian function confirm the first and second orders of Raman modes of the prepared compound. The activation energy value of  $E_a = 0.16$  eV obtained from the Arrhenius plot indicates the dielectric stability of the material. The photoluminescence study shows the excitation by the light from ultraviolet region (350 to 450 nm), exhibiting blue (355 nm) to  $^8\text{S}_{7/2} \rightarrow ^6\text{P}_{3/2}$  transition, which may provide new applications in the field of modern electronics.

## 1 Introduction

Rare earth-based double perovskites with the chemical formula of  $\text{R}_2\text{BB}'\text{O}_6$  (where R—rare-earth ions and B/B'—transition-metal ions) have gained

considerable interest in the field of technological applications and rudimentary research due to their fascinating properties like colossal magnetoresistance [1], multiferroicity [2–6] magnetocapacitance [7], magnetoelectric [8], magnetocaloric [9, 10] and

Address correspondence to E-mail: kskumar23@hotmail.com

energy storage devices [11]. In general, the double-perovskite compound is depicted as a 3-dimensional array of  $ABO_3$  and  $AB'O_3$  single perovskite units placed alternatively in space [12]. The distribution of ions in the B and B' cations at octahedral sites along with tilting of  $BO_6$  and  $B'O_6$  octahedra paves a path for phase stabilization of the double-perovskite compounds [13, 14]. Thus, the availability of cation at B-site is found useful in tuning of the desired application.

Among the rare-earth-based perovskites, the orthorhombic  $RMnO_3$  [15–17] and orthoferrite  $RFeO_3$  [18–20] are of significant importance in the field of multifunctional materials, due to their emerging magnetic and electrical properties. The position of a rare-earth element such as gadolinium in the A-site of a double-perovskite structure has received much attention due to its magnetocaloric effect and large magnetic moment. Recent reports on Gd-based double perovskites like  $Gd_2CoMnO_6$  and  $Gd_2NiMnO_6$  unleashed their magneto-dielectric effect and multifunctional properties. In the cobalt-substituted manganite  $Gd_2CoMnO_6$ , the interaction between the Co/Mn ions along with the Gd moments possesses 4f-3d negative magnetic interaction, which finds application towards the utilization of multi-ion magnetic ordering in the structure [21, 22]. The  $Gd_2CoMnO_6$  single crystals exhibit strong anisotropic magnetocaloric effect, which encourages the applied and fundamental research to achieve the functional properties [23]. The Sr ion doping at the A-site of  $Gd_2CoMnO_6$  is reported to enhance the magnetic entropy, magnetocaloric effect and ferromagnetic nature of the system [24]. Similarly, the nickel-substituted manganite  $Gd_2NiMnO_6$ , where the Co ions are replaced by Ni ions, exhibits an enhanced magneto-dielectric [25] and magnetocaloric effect of the system, making the material as a potential candidate for magnetic refrigerants application [26].

From a comprehensive literature survey, it is established that the synthesis and systematic analysis on  $Gd_2FeMnO_6$  compound are yet to be reported. Therefore, the present work is focussed on the preparation and characterization of novel  $Gd_2FeMnO_6$  double-perovskite compound. The results obtained from structural, magnetic and dielectric studies are also discussed for possible concurrence with the similar structures to obtain feasible applications.

## 2 Experimental

The polycrystalline  $Gd_2FeMnO_6$  compound was synthesized by high-temperature solid-state reaction method. The stoichiometric mixture of high-purity (purchased from Alfa Aesar) starting materials such as  $Gd_2O_3$ ,  $Mn_2O_3$  and  $Fe_2O_3$  were mixed thoroughly using an agate mortar. The well-ground mixture was placed in an alumina crucible and sintered at 1000 °C for 8 h with intermediate grindings. The obtained powder was finally sintered at 1100 °C for 12 h. Powder X-ray diffraction technique at room temperature was carried out with AERIS high-resolution X-ray diffractometer having  $CuK\alpha$  radiation (1.5406 Å) to find out the structural purity of the compound. The Rietveld refinement procedure has been involved with the support of FULLPROF software to obtain the structural parameters of the  $Gd_2FeMnO_6$  compound. The pseudo-Voigt function for peak fitting and 6-polynomial function for background fitting were employed for the structural analysis. X-ray photoelectron spectroscopy technique was carried out with the monochromatized Al-K $\alpha$  source at a base pressure of  $1.2 \times 10^{-7}$  Pa on the sample area of  $100 \mu m^2$  in PHI 5000 Versa Probe III Scanning XPS microscope for the identification of oxidation states of the elements present in the compound with the monochromatized Al-K $\alpha$  source at a base pressure of  $1.2 \times 10^{-7}$  Pa on the sample area of  $100 \mu m^2$ . The deconvolution and fitting of the elemental spectrum of Gd, Fe, Mn, C and O were performed using CASA XPS software, GL(30) fitting function with Shirley background. The etching of sample prior to measurement was not carried out, and a charge compensation current was allowed to pass through the sample during measurement. Raman spectral analysis was carried out using LabRAM HR (HORIBA) micro-Raman spectrometer with an excitation wavelength of 633 nm and Helium–Neon laser as a source in the spectral range of  $100\text{--}1000 \text{ cm}^{-1}$ . The scanning electron micrographs and elemental analysis were obtained using FEI Quanta 200 high-resolution scanning electron microscope instrument. The room-temperature photoluminescence spectrum was obtained using RF-530 IPC Shimadzu Spectro fluorophotometer. The magnetization (M–H curve) measurement has been carried out with Lakeshore VSM 7410S instrument. Dielectric measurements in the frequency range of 10 Hz to 1 MHz were recorded at different temperatures using Wayne Kerr LCR 4275 m instrument.

### 3 Results and discussion

#### 3.1 X-ray photoelectron spectroscopy (XPS) analysis

The X-ray photoelectron spectroscopy analysis was carried out to determine the oxidation states of the elements present in the prepared stoichiometric compound. Figure 1a and b shows the C1s and O1s fitting of Gd<sub>2</sub>FeMnO<sub>6</sub> compound. Figure 1c shows the survey spectrum of Gd<sub>2</sub>FeMnO<sub>6</sub> which confirms the presence of Gd, Fe, Mn and O elements in the prepared compound. The fitting of elemental spectrum was carried out using CASA XPS software and the fitting parameters and is listed in Tables 1 and 2. Table 1 reveals the binding-energy values obtained for C1s and O1s spectrum, which indicates the absence of adventitious carbon from the analysed sample [27]. This is evident from the values obtained for C–C and Fe–C bonds, as listed in Table 1. Therefore, no charge correction was carried out for the binding-energy values obtained for the elements Gd, Fe and Mn, as listed in Table 2. The Gd-4d, Mn-2p and Fe-2p spectra of Gd<sub>2</sub>FeMnO<sub>6</sub> compound are shown in Fig. 1d–f. The binding-energy values of 142.4 eV and 146.6 eV obtained from the fitting of Gd-4d<sub>5/2</sub> and Gd-4d<sub>3/2</sub> peaks, respectively, in the Gd spectrum indicate the presence of Gd<sup>3+</sup> ions in the structure, as reported for Gd<sub>2</sub>O<sub>3</sub>. The fitting of Fe-2p<sub>3/2</sub> and Fe-2p<sub>1/2</sub> peaks in the Fe spectrum yields the values of 712.4 eV for and 725.9 eV, respectively, which matches well with the values reported for Fe<sub>2</sub>O<sub>3</sub> compound [28]. Similarly, the Mn ion exists in + 3 oxidation states with the binding-energy value of 641.4 eV for Mn-2p<sub>3/2</sub> and 653.05 eV for Mn-2p<sub>1/2</sub> that again coincides with the binding-energy values reported for Mn<sub>2</sub>O<sub>3</sub> with Mn<sup>3+</sup> ions. These binding-energy values obtained from fitting for Gd, Fe and Mn ions are listed in Table 2. Hence, the existence of Mn, Fe and Gd ions in the + 3 oxidation states demonstrates the phase stabilization of the obtained Gd<sub>2</sub>FeMnO<sub>6</sub> double-perovskite system.

#### 3.2 Phase and microstructure analysis

The Rietveld refinement was carried out using FULLPROF program to obtain the structural parameters of polycrystalline double-perovskite Gd<sub>2</sub>FeMnO<sub>6</sub> compound [29]. The refinement was performed by fixing the structural features of GdFeO<sub>3</sub>

phase as a starting model with the incorporation of Mn ions into the system. Further, the random distribution of Fe and Mn ions in the B and B' sites of R<sub>2</sub>BB'O<sub>6</sub> double-perovskite structure leads to the occurrence of the disordered double perovskite system. The comparable ionic radii of the Fe<sup>3+</sup> (0.55 Å) and Mn<sup>3+</sup> (0.58 Å) ions are also to be found responsible for the crystalline phase stabilization of the double-perovskite system [30]. Figure 2a shows the Rietveld refinement pattern of the Gd<sub>2</sub>FeMnO<sub>6</sub> compound along with the powder X-ray diffraction data obtained at room temperature. The schematic representation of Gd<sub>2</sub>FeMnO<sub>6</sub> crystal structure is shown in Fig. 2b, where the Gd<sup>3+</sup> ions occupy the 4c Wyckoff position, Fe<sup>3+</sup>/Mn<sup>3+</sup> ions occupy the 4b Wyckoff positions and the O<sup>2-</sup> ions occupy 4c and 8d Wyckoff positions. The Rietveld refinement analysis confirms the formation of single-phase Gd<sub>2</sub>FeMnO<sub>6</sub> double-perovskite compound which crystallizes in orthorhombic structure and belonging to *Pbmm* space group. Hence, the assumption of alternate ordering of GdFeO<sub>3</sub> and GdMnO<sub>3</sub> unit cells to form the double-perovskite structure of Gd<sub>2</sub>FeMnO<sub>6</sub> is proved through XPS and powder XRD data analysis. The structural parameters obtained from the Rietveld refinement process are listed in Table 3. The bond angles and the bond distance values calculated using the structural parameters obtained from the refinement are listed in Table 4. The stability of perovskites compounds with the chemical formula of ABO<sub>3</sub> is estimated using the tolerance factor expression:

$$T_F = \frac{R_{Gd} + R_O}{\sqrt{2} \left[ \frac{R_{Fe}}{2} + \frac{R_{Mn}}{2} + R_O \right]},$$

where  $R_{Gd}$ ,  $R_{Fe}$ ,  $R_{Mn}$  and  $R_O$  are the ionic radii of Gd<sup>3+</sup>, Fe<sup>3+</sup>, Mn<sup>3+</sup> and O<sup>2-</sup> ions [31]. The calculated value of tolerance factor is found to be  $t = 0.85$ , which indicates the support for the stabilization of double-perovskite orthorhombic structure. Here, the tolerance factor is dependent on the radius of A and B cations in the perovskites which are critical for the formation of the structure. The value of tolerance factor between 0.8 and 1.0 provides a better stability for formation of perovskite structure. Values other than this range of tolerance factor lead to less stable or non-perovskite structures.

The surface morphology of the prepared compound was analysed using high-resolution scanning electron microscopy technique, and the micrographs are shown in Fig. 3. From the micrographs, it is

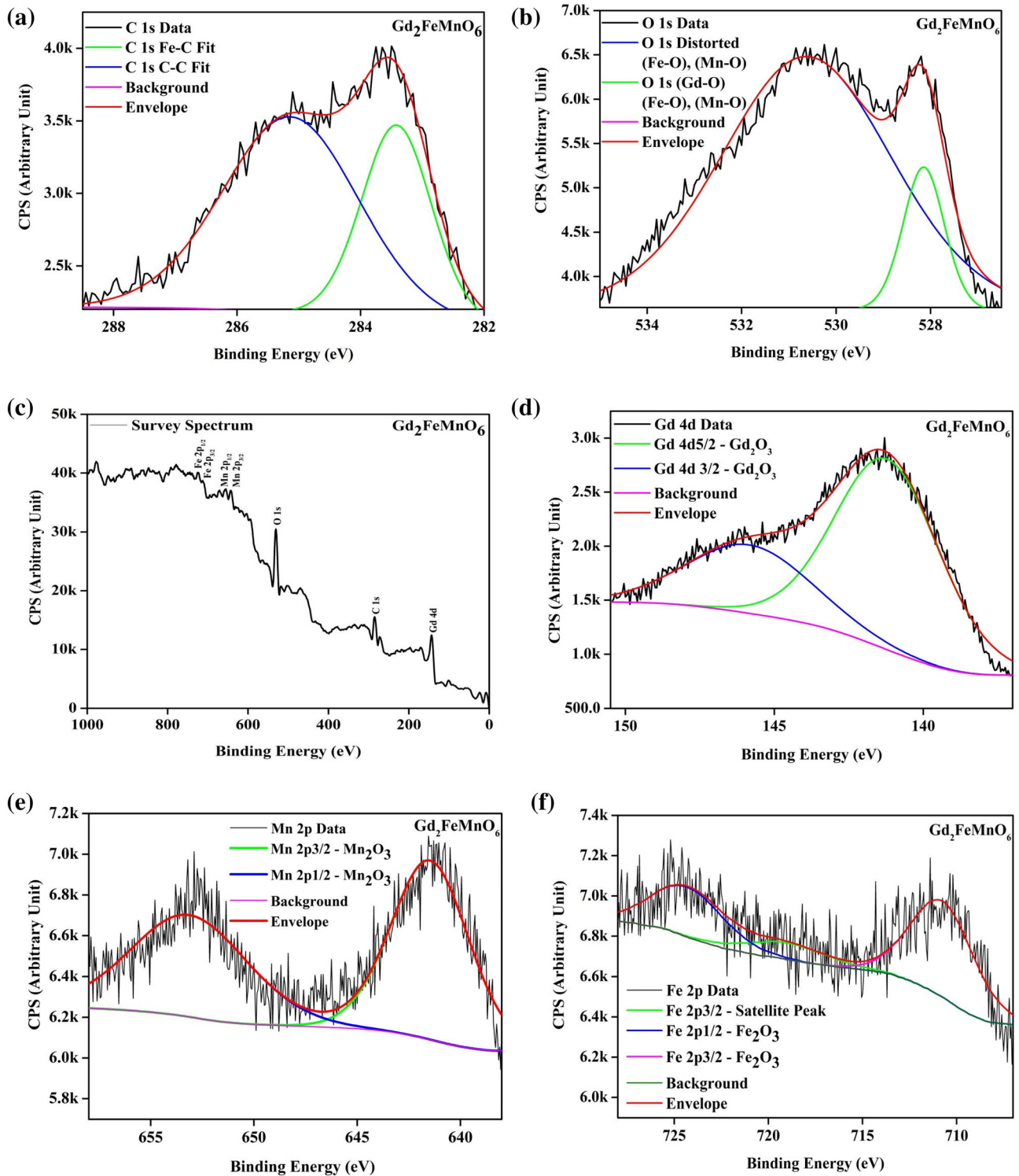


**Fig. 1** The XPS spectrum of **a** C1s and **b** O1s of  $Gd_2FeMnO_6$  is shown. The **c** survey spectrum, **d** Gd, **e** Mn and **f** Fe are also shown from the compound  $Gd_2FeMnO_6$

observed that the grains are randomly distributed with dense agglomeration. Further, the energy dispersive spectral analysis (EDS) of  $Gd_2FeMnO_6$

reveals the presence of Gd, Fe, Mn and O elements and confirms the purity of the compound.

**Table 1** Binding-energy values of C1s and O1s spectrum of Gd<sub>2</sub>FeMnO<sub>6</sub>

C 1s Fit	Gd <sub>2</sub> FeMnO <sub>6</sub>	O 1s Fit	Gd <sub>2</sub> FeMnO <sub>6</sub>
Fe–C	283.16 (32%)	M–O	528.83 (16%)
C–C (284.8 eV)	285.61 (68%)	M–O	530.32 (59%)
C–O–C (~ 286 eV)	–	M–O	532.46 (25%)
O–C=O (288.5 eV)	–	C=O	–
		C–O	–

**Table 2** Binding-energy values of elements obtained from XPS spectrum of Gd<sub>2</sub>FeMnO<sub>6</sub>

	Gd <sub>2</sub> FeMnO <sub>6</sub> <sup>a</sup> (eV)
C 1s	285.61
O 1s	530.60
Gd-4d5/2	141.38
Mn-2p3/2	641.50
Fe-2p3/2	710.90

<sup>a</sup>The values of Binding Energy as obtained from curve fitting of experimental data

### 3.3 Raman analysis

Figure 4 shows the room-temperature Raman spectra of the prepared Gd<sub>2</sub>FeMnO<sub>6</sub> compound that was fitted using Lorentzian functions to identify the Raman-active modes. Experimentally observed Raman-active modes are assigned to the corresponding phonon mode with the help of lattice dynamical calculations reported earlier, as listed in Table 5 [32]. Based on the group theory calculations, the possible zone-centre lattice modes of vibrations of the double-perovskite compounds are given below:

$$\Gamma_{\text{Pbnm}} = 7A_g + 7B_{1g} + 5B_{2g} + 5B_{3g} + 8A_u + 10B_{1u} + 8B_{2u} + 10B_{3u}.$$

Among them, there are 24 Raman-active modes  $\Gamma = 7A_g + 7B_{1g} + 5B_{2g} + 5B_{3g}$ , 25 infrared-active (IR) modes  $\Gamma = 9B_{1u} + 7B_{2u} + 9B_{3u}$ , 3 translational modes  $B_{1u} + B_{2u} + B_{3u}$  and 8 Raman inactive modes ( $8A_u$ ) present. In polarized Raman scattering, the  $A_g$  modes can be observed by parallel polarization, while the  $B_g$  modes can be observed by both parallel and crossed polarizations. Since all these modes fall in the frequency range below  $\sim 1000 \text{ cm}^{-1}$ , most of the Raman studies have been focussed in this region. The spectrum of the Gd<sub>2</sub>FeMnO<sub>6</sub> compound exhibits

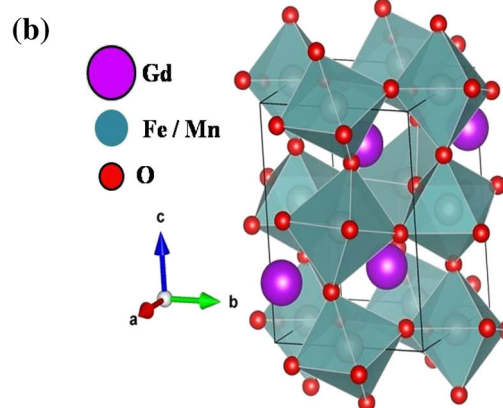
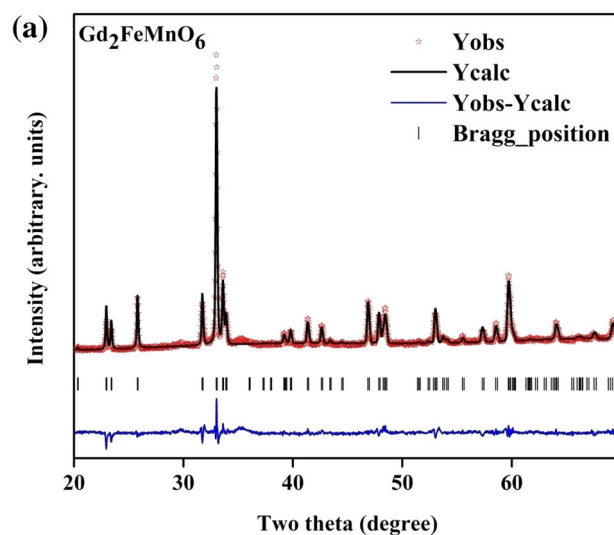


**Fig. 2** **a** The Rietveld Refinement of the room-temperature X-ray diffraction pattern obtained for the Gd<sub>2</sub>FeMnO<sub>6</sub> compound. **b** The schematic representation of orthorhombic crystal structure of Gd<sub>2</sub>FeMnO<sub>6</sub>

**Table 3** Lattice and structural parameters of Gd<sub>2</sub>FeMnO<sub>6</sub> obtained from the Rietveld refinement of the XRD data

Atom	Site	x	y	Z	Occupancy
Gd	4c	0.9850	0.0630	0.2500	1.0
Mn/Fe	4b	0.5	0.0	0.0	0.5/0.5
O1	4c	0.1120	0.4570	0.2500	1.0
O2	8d	0.6960	0.3020	0.0520	1.0

$$a = 5.3226(2) \text{ \AA}, b = 5.6396(3) \text{ \AA}, c = 7.5992 \text{ \AA}(2), V = 228 \text{ \AA}^3$$

$$\chi^2 = 4.230, R_{\text{exp}} = 1.45\%, R_p = 1.58\%, R_{\text{wp}} = 2.23\%$$

vibrational modes at 135, 239, 298, 385, 613, 832, 908 and 962  $\text{cm}^{-1}$ . Among them, four first-order modes (135, 239, 298 and 385  $\text{cm}^{-1}$ )  $A_g$  and two first-order (613 and 832  $\text{cm}^{-1}$ )  $B_g$  Raman-active phonons are

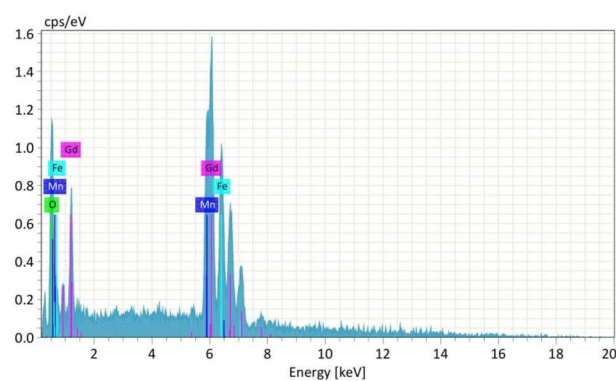
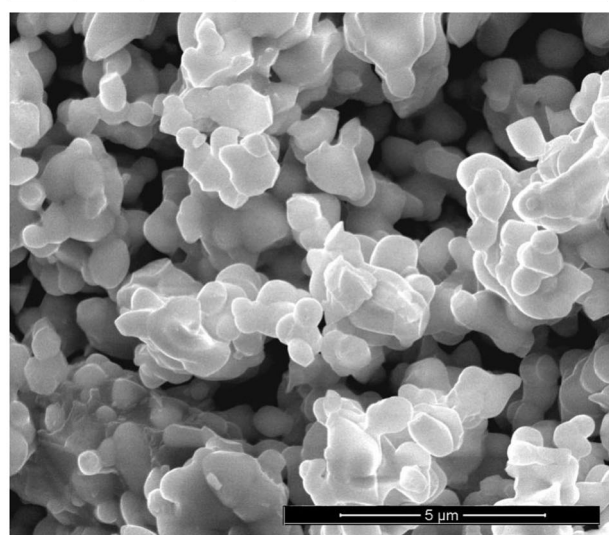
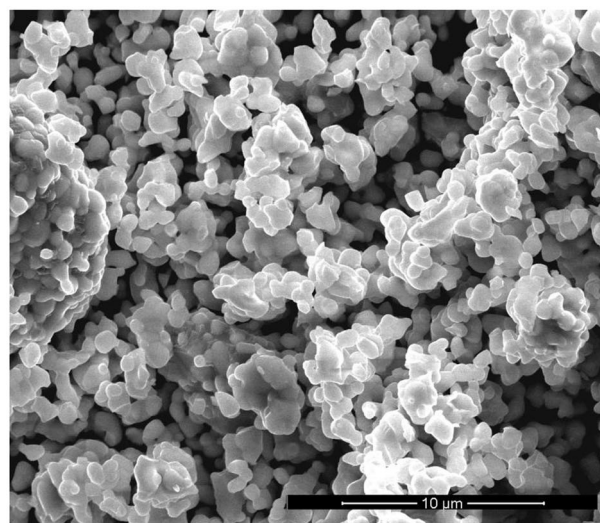
**Table 4** Bond angle and bond distances of  $\text{Gd}_2\text{FeMnO}_6$ 

Bond angles		Bond distances	
Chain	Angle ( $^\circ$ )	Bond	Distance (in $\text{\AA}$ )
Fe/Mn–O1–Fe/Mn	158	Gd–O	2.46
Fe/Mn–O2–Fe/Mn	151	Fe/Mn–O	1.94
Fe–O1–Mn	158		
Fe–O2–Mn	151		
Gd–O1–Fe/Mn	93		
Gd–O2–Fe/Mn	92		

detected [33–36]. Remaining two vibrational modes attribute in the second-order modes at 908 and 962  $\text{cm}^{-1}$   $2B_g$ . Most of the bands are weak; Moreover, some weak bands are most likely overlapped by much stronger bands, Furthermore, the frequencies of the 239  $\text{cm}^{-1}$   $A_g$  mode and 298  $\text{cm}^{-1}$   $A_g$  mode exhibit a weak band [37] whereas the frequencies of the 135  $\text{cm}^{-1}$   $A_g$  mode and 613  $\text{cm}^{-1}$   $B_g$  modes show a strong band. These strong Raman-active band values are in good agreement with those reported by Romaguerabarcelay et al. [33].

### 3.4 Photoluminescence studies

The photoluminescence excitation and emission spectra of the  $\text{Gd}_2\text{FeMnO}_6$  compound are shown in Fig. 5. The emission spectra of the compound are having peaks at 470 nm, 517 nm and 594 nm, respectively. As of the literature, the emission wavelengths are mainly attributed to the transition of  $\text{Gd}^{3+}$  ions,  ${}^2F_{7/2} \rightarrow {}^4I_{15/2}$ ,  ${}^6G_{7/2} \rightarrow {}^4I_{15/2}$  and  ${}^6G_{13/2} \rightarrow {}^4I_{15/2}$  [38]. But the prepared compound shows peaks that are weak compared to the reported results, and the broad intense emission peak centred at 470 nm has not been reported; yet the prepared compound has been excited by UV radiation at an optimal wavelength of 355 nm ( ${}^8S_{7/2} \rightarrow {}^6P_{3/2}$ ). This wavelength corresponds to the maximum of the wide band that is linked with charge transfer between the  $\text{O}^{2-}$  and  $\text{Gd}^{3+}$  ions. Less intense peaks around 460 and 600 nm are due to the energy transfer from Gd to Fe and Mn to the f-d transitions ions, and  $\text{Gd}^{3+}$  ion exhibits two bands in the blue (450–495 nm) and green (495–570 nm) regions [39]. When  $\text{Gd}^{3+}$  ion is located at low symmetry local site (without inversion symmetry), the green emission is dominant in the emission spectrum, whereas when  $\text{Gd}^{3+}$  is presented

**Fig. 3** SEM and EDS images of  $\text{Gd}_2\text{FeMnO}_6$  compound

at a high symmetry local site (with inversion symmetry), the blue emission is stronger than the green emission [40].

The schematic energy level diagram for the optical transitions and the emissions spectra corresponds to

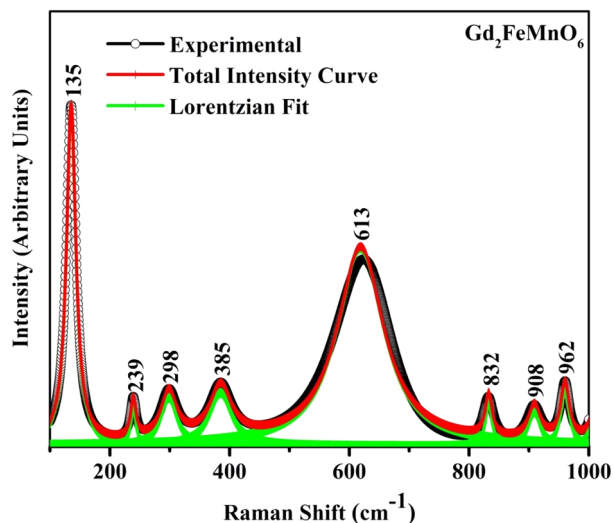


**Fig. 4** Raman-active region of  $\text{Gd}_2\text{FeMnO}_6$  compound

the transition between  ${}^2F_{7/2} \rightarrow {}^4I_{15/2}$ ,  ${}^6G_{7/2} \rightarrow {}^4I_{15/2}$  and  ${}^6G_{13/2} \rightarrow {}^4I_{15/2}$ , respectively, as is shown in Fig. 6 [41]. As per the combination of elements, the emission bands are contributed by the localized energy levels of rare-earth and transition-metal ions.

### 3.5 Magnetic property

The magnetization analysis for the title compound has been carried out at room temperature, and the resultant is shown in Fig. 7. From the graph, it is noted that the magnetization behaviour of  $\text{Gd}_2\text{FeMnO}_6$  compound is dominated by the exchange interaction of Fe/Mn–O–Fe/Mn ions that leads to antiferromagnetic behaviour of the compound with

weak ferromagnetic ordering [42]. The magnetic interactions between  $\text{Fe}^{3+}$  and  $\text{Mn}^{3+}$  ions are quite complex due to the random distribution of B and B' ions that gives rise to the super-exchange chains such as  $\text{Fe}^{3+}\text{--O}^{2-}\text{--Fe}^{3+}$ ,  $\text{Mn}^{3+}\text{--O}^{2-}\text{--Mn}^{3+}$  and  $\text{Fe}^{3+}\text{--O}^{2-}\text{--Mn}^{3+}$ . Therefore, the following exchange interaction chains are possibly formed in the double-perovskite structure [14]:

- (i)  $\text{Fe}^{3+}\text{--O}^{2-}\text{--Fe}^{3+}$  (J1)
- (ii)  $\text{Mn}^{3+}\text{--O}^{2-}\text{--Mn}^{3+}$  (J2)
- (iii)  $\text{Fe}^{3+}\text{--O}^{2-}\text{--Mn}^{3+}$  (J3)

As per the literature survey, it is to be considered that the chains J1 and J2 may give rise to antiferromagnetic ordering due to the super-exchange magnetic interaction between the magnetic ions of same type and amount of valency like  $\text{Fe}^{3+}$  and  $\text{Mn}^{3+}$ . Further, the combination of ions with mixed oxidation state leads to ferromagnetic interaction resulting from the double-exchange interaction in J3 chain. Hence, the antiferromagnetic interactions predominate in the structure with a greater number of J1 and J2 chains. It is also to be noted that few of layers of J2 ferromagnetic chains also contribute to the observed magnetic behaviour at lower applied magnetic field in connection with the mixed double-perovskite arrangement of  $\text{Fe}^{3+}$  ions and  $\text{Mn}^{3+}$  ions in the host lattice matrix. The long chains of alternative and mixed  $\text{Fe}^{3+}/\text{Mn}^{3+}$  ions in association with  $\text{Gd}^{3+}$  spins frame the magnetic structure of the compound [43]. As the B-site ions are disordered, complex magnetic interactions exist in the system.

**Table 5** Symmetry assignment of Raman modes for the observed peaks

Raman shift ( $\text{cm}^{-1}$ )		Assignment of modes
Experimental	References [28–32]	
135	134	$A_g$
239	245	$A_g$
298	301	$A_g$
385	385	$A_g$
613	613	$B_g$
832	(The modes observed at 832, 908 and 962 $\text{cm}^{-1}$ are assigned to the stretching vibration modes in Fe–O–Mn sublattices)	In this work (see text)
908	–	In this work (see text)
962	–	In this work (see text)

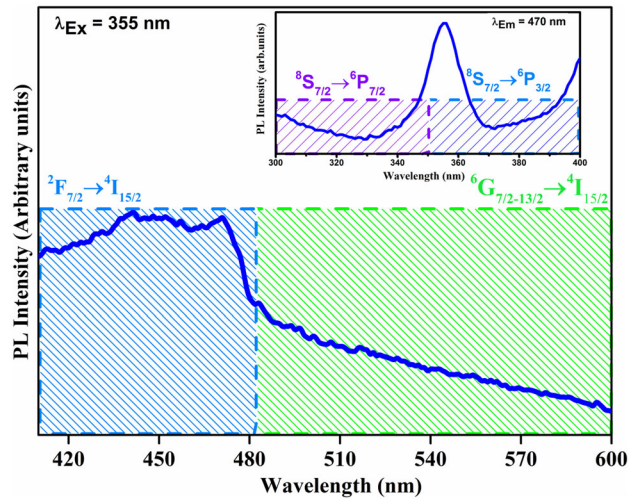


**Fig. 5** Photoluminescence emission and excitation spectra of  $Gd_2FeMnO_6$  compound

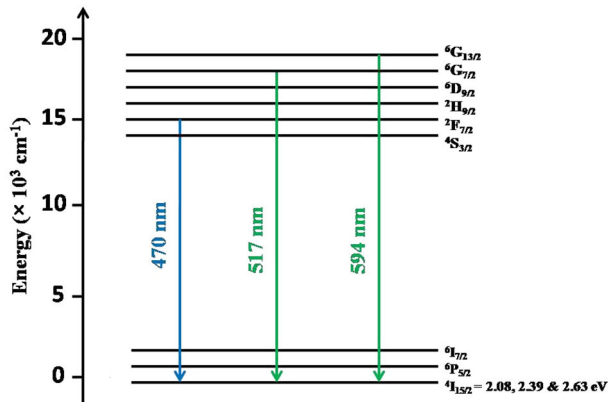


**Fig. 6** Energy level diagram and emission transitions of  $Gd_2FeMnO_6$  compound

The super-exchange chains, Fe/Mn–O–Fe/Mn, play a major role in determining the magnetic nature of the materials. The bond angles and bond distance of most iteration of ions are listed in Table 4. According to Goodenough Kanamori Anderson rules, the Fe/Mn–O–Fe/Mn bond angles of about 155 degrees give rise to competing antiferromagnetic and ferromagnetic ordering [42–44]. This is in agreement with the argument based on the J1, J2 and J3 chains. Based on the local alignment of spins ( $Mn^{3+}$  and  $Fe^{3+}$ ) in the particular region of compound, the external magnetic field tends to align the spins in the antiferromagnetic order. This leads to the observed behaviour of the weak ferromagnetic ordering at low applied external magnetic field which is slowly disappearing with increase in the magnetic field values.

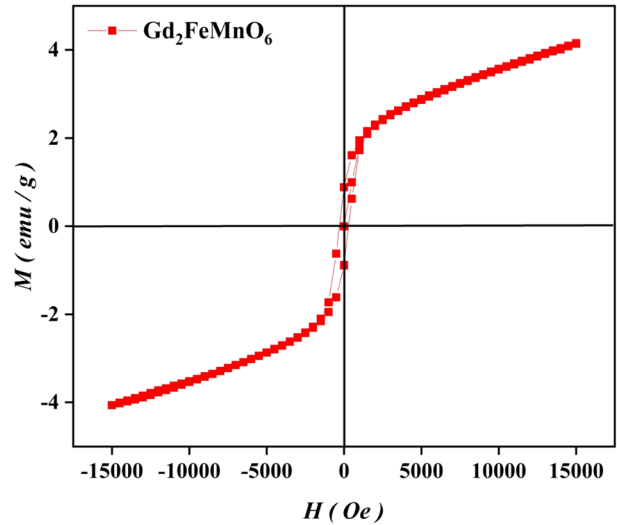


**Fig. 7** Room-temperature magnetization curves obtained for  $Gd_2FeMnO_6$  compound

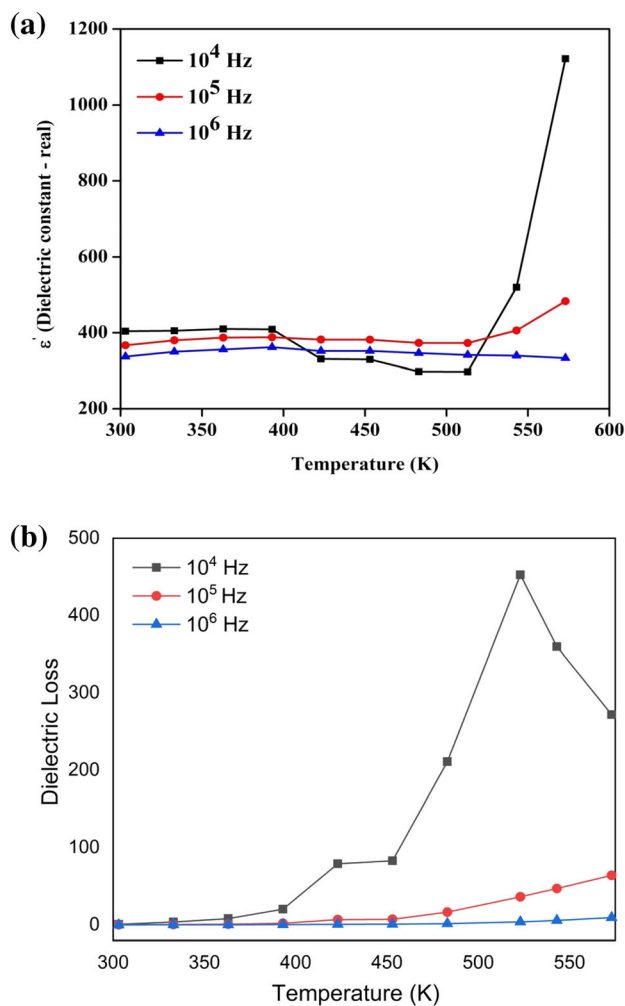
### 3.6 Dielectric analysis

Figure 8a shows the temperature dependence dielectric constant plot with different frequencies. It is observed that the values of dielectric constant show no variation till 510 K approximately, above which there is an increase in the observed values of dielectric constant. Figure 9a represents the frequency dependence dielectric constant graph with varied temperatures. It is found that the dielectric constant value decreases with increasing frequency. The Arrhenius plot used for the determination of activation energy ( $E_a$ ) is shown in Fig. 10. From the linear fitting and by the use of straight-line equation, the activation energy is obtained and found to be 0.16 eV. The resistivity plot of  $Gd_2FeMnO_6$  indicates a decrease in resistivity with increasing temperature.

Dielectric loss factor is a significant measurement to identify the total core loss in ferrites. Hence for low core loss, low dielectric losses are desirable. Further, the dielectric loss factor  $\tan\delta$  represents the dissipation of input electric energy in the dielectric system. The variation of  $\tan\delta$  as a function of frequency at room temperature is shown in Figs. 8b and 9b.

It is observed that for all the samples, the dielectric loss decreases continuously with increasing frequency. A maximum value of  $\tan\delta$  is observed when the jump frequency of electron between  $Fe^{2+}$  and  $Fe^{3+}$  is equal to the frequency of the applied field. Thus, the dielectric loss factor of the  $Gd_2FeMnO_6$





**Fig. 8** **a** Temperature-dependent dielectric constant plot, and **b** Dielectric loss plot of  $Gd_2FeMnO_6$  at different frequencies

compound is expected to decrease approximately inverse to the frequency [45].

From Fig. 8b, it is observed that the increase in frequency of electric signal leads to gradual increase in dissipation loss whereas for the input frequency of  $10^4$  Hz, the variations are observed at high temperatures due to abnormal singularities of the polarization behaviour. The frequency-dependant dielectric loss plot also exhibits the unique singularity polarization nature of the prepared compound irrespective of the temperature supplied to the compound. Hence, the dielectric studies reveal the possibility of developing highly polarizable double-perovskite-structured compound for futuristic applications.

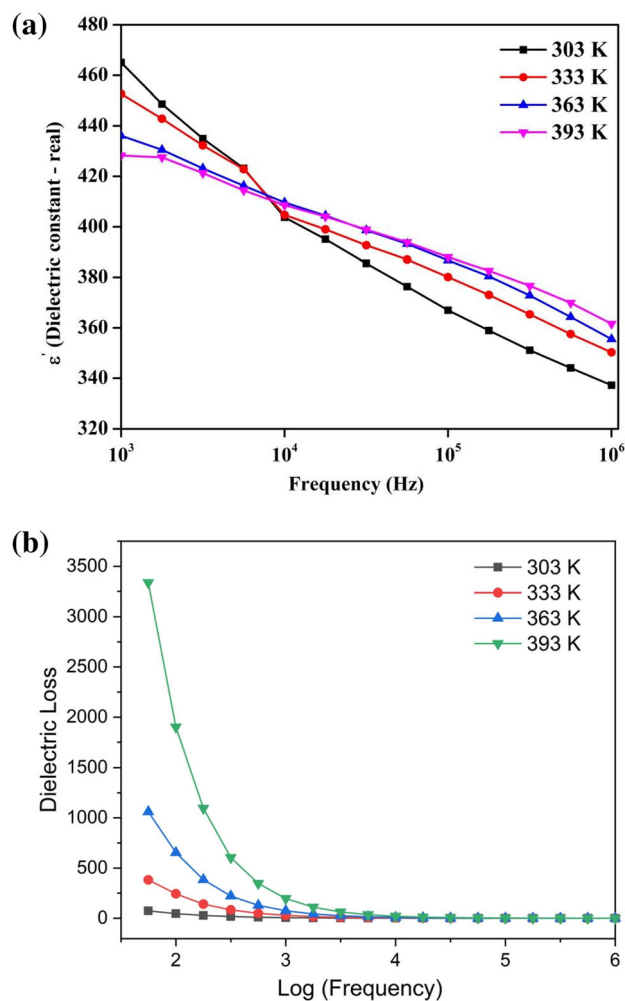


**Fig. 9** **a** Frequency-dependent dielectric constant plot, and **b** Dielectric loss plot of  $Gd_2FeMnO_6$  at different temperatures

## 4 Conclusion

To summarize, polycrystalline  $Gd_2FeMnO_6$  double-perovskite compound has been synthesized by high-temperature solid-state reaction technique. The Rietveld refinement process on powder X-ray diffraction data shows that the compound crystallizes in an orthorhombic structure with  $Pbnm$  space group. X-ray photoelectron spectroscopy confirms the +3 oxidation state of the elements present in the compound. Raman spectra recorded at room temperature reveals that the  $A_g$  and  $B_g$  Raman modes in the range of  $100\text{--}1000\text{ cm}^{-1}$  were observed for  $Gd_2FeMnO_6$  compound. The observed emission spectra recorded with the excitation of wavelength 355 nm show three strong broad emission bands at about 470, 517 and 594 nm for the prepared compound. Room-

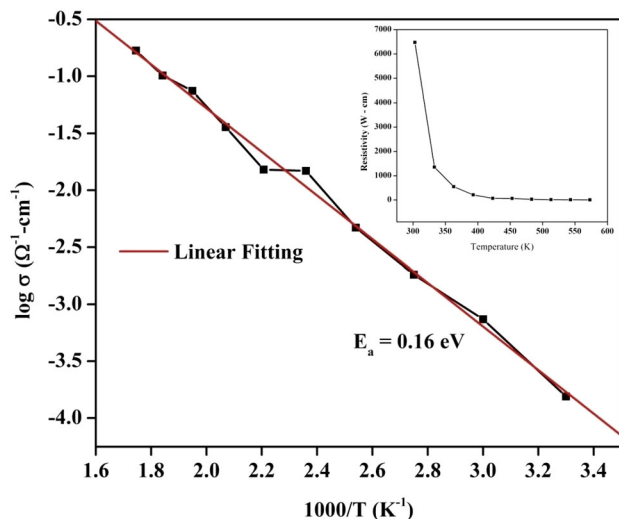


**Fig. 10** Arrhenius plot for the determination activation energy of  $\text{Gd}_2\text{FeMnO}_6$  (Inset: Resistivity plot obtained from dielectric measurements)

temperature hysteresis loop shows the antiferromagnetic behaviour of the compound with weak ferromagnetic interactions. The dielectric study with respect to temperature and frequency reveals the conduction process with activation energy of 0.16 eV. These results suggest the compound to be a potential candidate for modern electronics, magneto-optical storage and optical materials like opto-electronic and sensor devices.

## Acknowledgement

The Author J. Stella Punitha thanks SRM IST for their support through fellowship. The authors thankfully acknowledge Nanotechnology Research Centre (NRC), SRMIST for providing characterization facilities such as XPS, XRD and VSM.

## Declarations

**Conflict of interest** All authors have participated in (a) conception and design, or analysis and interpretation of the data; (b) drafting the article or revising it critically for important intellectual content and (c) approval of the final version. This manuscript has not been submitted to, nor is under review at, another journal or other publishing venue. The authors have no affiliation with any organization with a direct or indirect financial interest in the subject matter discussed in the manuscript.

## References

1. S. Yamada, N. Abe, H. Sagayama, K. Ogawa, T. Yamagami, T. Arima, *Phys. Rev. Lett.* **123**, 126602 (2019)
2. H.J. Zhao, W. Ren, Y. Yang, J. Íñiguez, X.M. Chen, L. Bellaiche, *Nat. Commun.* **5**, 1 (2014)
3. M. Ležaić and N. A. Spaldin, *Phys. Rev. B Condens. Matter Mater. Phys.* **83**, (2011).
4. T.Y. Cai, S.C. Liu, S. Ju, C.Y. Liu, G.Y. Guo, *Phys. Rev. Appl.* **8**, 1 (2017)
5. Y. Tokunaga, S. Iguchi, T. Arima, Y. Tokura, *Phys. Rev. Lett.* **101**, 3 (2008)
6. Y. Tokunaga, N. Furukawa, H. Sakai, Y. Taguchi, T.H. Arima, Y. Tokura, *Nat. Mater.* **8**, 558 (2009)
7. M. Das, P. Sarkar, P. Mandal, *Phys. Rev. B* **101**, 144433 (2020)
8. M.K. Kim, J.Y. Moon, S.H. Oh, D.G. Oh, Y.J. Choi, N. Lee, *Sci. Rep.* **9**, 1 (2019)
9. T. Chakraborty, H. Nhalil, R. Yadav, A.A. Wagh, S. Elizabeth, *J. Magn. Magn. Mater.* **428**, 59 (2017)
10. L. Su, X.Q. Zhang, Q.Y. Dong, Y.J. Ke, K.Y. Hou, C.S. Liu, Z.H. Cheng, *J. Alloys Compd.* **746**, 594 (2018)
11. C. Chappert, A. Fert, F.N. Van Dau, *Nat. Mater.* **6**, 813 (2007)
12. A. Hossain, P. Bandyopadhyay, S. Roy, *J. Alloys Compd.* **740**, 414 (2018)
13. M.T. Anderson, K.B. Greenwood, G.A. Taylor, K.R. Poepelmeier, *Prog. Solid State Chem.* **22**, 197 (1993)
14. S. Abhirami and S. S. Basha, *J. Mater. Sci. Mater. Electron.* **1** (2021).
15. X.L. Wang, D. Li, T.Y. Cui, P. Kharel, W. Liu, Z.D. Zhang, *J. Appl. Phys.* **107**, 766 (2010)
16. S. Samantaray, D.K. Mishra, S.K. Pradhan, P. Mishra, B.R. Sekhar, D. Behera, P.P. Rout, S.K. Das, D.R. Sahu, B.K. Roul, *J. Magn. Magn. Mater.* **339**, 168 (2013)
17. A. Pal and P. Murugavel, *J. Appl. Phys.* **123**, (2018).
18. M. Das, S. Roy, P. Mandal, *Phys. Rev. B* **96**, 1 (2017)
19. A.T.S. Sudandararaj, G. Sathish Kumar, M. Dhivya, R.D. Eithiraj, I.B.S. Banu, *J. Alloys Compd.* **783**, 393 (2019)
20. X.H. Zhu, X.B. Xiao, X.R. Chen, B.G. Liu, *RSC Adv.* **7**, 4054 (2017)
21. J.K. Murthy, A. Venimadhav, *J. Alloys Compd.* **719**, 341 (2017)
22. R.C. Sahoo, S. Das, T.K. Nath, *J. Magn. Magn. Mater.* **460**, 409 (2018)
23. J.Y. Moon, M.K. Kim, Y.J. Choi, N. Lee, *Sci. Rep.* **7**, 1 (2017)
24. R.C. Sahoo, S. Das, T.K. Nath, *J. Appl. Phys.* **124**, 1 (2018)
25. S. H. Oh, H. Y. Choi, J. Y. Moon, M. K. Kim, Y. Jo, N. Lee, and Y. J. Choi, *J. Phys. D: Appl. Phys.* **48**, (2015).

26. J. Krishna Murthy, K. Devi Chandrasekhar, S. Mahana, D. Topwal, A. Venimadhav, J. Phys. D. Appl. Phys. **48**, 355001 (2015)
27. G. Greczynski, L. Hultman, Prog. Mater. Sci. **107**, 100591 (2020)
28. D. Briggs, *Handbook of Adhesion*, 2nd edn. (Wiley, New York, 2005), p. 621
29. H.M. Rietveld, J. Appl. Crystallogr. **2**, 65 (1969)
30. P. Hartman and H. K. Chan, Pharm. Res. An Off. J. Am. Assoc. Pharm. Sci. **10**, 1052 (1993).
31. M. Dhilip, N.A. Devi, J.S. Punitha, V. Anbarasu, K.S. Kumar, Vacuum **167**, 16 (2019)
32. L. Martín-Carrón, A. De Andrés, Eur. Phys. J. B **22**, 11 (2001)
33. Y. Romaguera-Barcelay, J. Agostinho-Moreira, A. Almeida, P.B. Tavares, J. Pérez De La Cruz, Thin Solid Films **564**, 419 (2014)
34. R.J. Wiglusz, K. Kordek, M. Małecka, A. Ciupa, M. Ptak, R. Pazik, P. Pohl, D. Kaczorowski, Dalt. Trans. **44**, 20067 (2015)
35. P. Negi, G. Dixit, H.M. Agrawal, H. Kumar, R.C. Srivastava, P.C. Sati, V. Gupta, K. Asokan, Ferroelectrics **519**, 200 (2017)
36. A. Panchwane, V.R. Reddy, A. Gupta, V.G. Sathe, Mater. Chem. Phys. **196**, 205 (2017)
37. S. Mansouri, S. Jandl, A. Mukhin, V.Y. Ivanov, A. Balbashov, Sci. Rep. **7**, 1 (2017)
38. Y. Zhang, A. Zheng, X. Yang, H. He, Y. Fan, C. Yao, CrystEngComm **14**, 8432 (2012)
39. R.K. Tamrakar, D.P. Bisen, N. Brahme, Res. Chem. Intermed. **40**, 1771 (2014)
40. R.K. Tamrakar, D.P. Bisen, N. Brahme, J. Radiat. Res. Appl. Sci. **7**, 550 (2014)
41. C. Balamurugan, S.J. Song, D.W. Lee, Sens. Actu. B Chem. **272**, 400 (2018)
42. J.B. Goodenough, Phys. Rev. **100**, 564 (1955)
43. J. Kanamori, J. Phys. Chem. Solids **10**, 87 (1959)
44. P.W. Anderson, Phys. Rev. **79**, 350 (1950)
45. V. Anbarasu, P.M. Md Gazzali, T. Karthik, A. Manigandan, K. Sivakumar, J. Mater. Sci. Mater. Electron. **24**, 916 (2013)

**Publisher's Note** Springer Nature remains neutral with regard to jurisdictional claims in published maps and institutional affiliations.